Title
Effects on precipitation, clouds, and temperature from long-range transport of idealized aerosol plumes in WRF-Chem simulations

Journal
Journal of Geophysical Research, 117(D5)

ISSN
0148-0227

Authors
Zhao, Zhan
Pritchard, Michael S
Russell, Lynn M

Publication Date
2012-03-03

DOI
10.1029/2011JD016744

Effects on precipitation, clouds, and temperature from long-range transport of idealized aerosol plumes in WRF-Chem simulations

Zhan Zhao,[1] Michael S. Pritchard,[1] and Lynn M. Russell[1]

Received 19 August 2011; revised 7 December 2011; accepted 27 December 2011; published 3 March 2012.

[1] Using the Weather Research and Forecasting model with Chemistry (WRF-Chem), we explored the impacts of nonlocal aerosol plumes transported at three different altitudes on a summertime convective system developed in a clean environment over the northeastern United States. Idealized aerosol plumes from forest fire and volcano emissions, which are known to be frequently transported in this region, were prescribed at three separate altitudes on the upstream boundary of WRF-Chem. The low-altitude (1.5–2.5 km) plume characteristic of forest fire emissions intersects the water clouds, resulting in optically thicker clouds and about a 30% decrease in accumulated precipitation. The precipitation response to the idealized aerosol plume is attributed to the aerosol "second indirect effect" and aerosol-induced enhancement in evaporation efficiency. Convection also significantly impacted this low-altitude aerosol plume because wet removal scavenges up to 70% of plume aerosols over regions where deep convection and precipitation occur. In stark contrast, midaltitude (5.6–6.6 km) and high-altitude (11.5–12.5 km) plumes exerted a negligible effect on clouds and precipitation. The apparent highly nonlinear sensitivity of simulated convection to the vertical positioning of nonlocal aerosol plumes is explained in terms of the dominant controls influencing this convection regime and limitations in the microphysics currently implemented in WRF-Chem.

Citation: Zhao, Z., M. S. Pritchard, and L. M. Russell (2012), Effects on precipitation, clouds, and temperature from long-range transport of idealized aerosol plumes in WRF-Chem simulations, *J. Geophys. Res.*, *117*, D05206, doi:10.1029/2011JD016744.

1. Introduction

[2] Effects from long-range transport of aerosols on regional hydrometeorology are poorly understood. Although high-resolution mesoscale modeling systems now include many physical and chemical processes, pollution plumes originating outside the modeled domain are not typically included in regional simulations [e.g., *Giorgi et al.*, 2002, 2003; *Huang et al.*, 2007; *Chapman et al.*, 2009; *Ntelekos et al.*, 2009]. Analysis is instead confined to aerosol-cloud interactions from local pollution and the resulting effects on clouds and climate. Such studies have shown that depending on convection regime and environmental conditions, the precipitation response to an increase in local aerosol loading can be either suppression or enhancement [*Rosenfeld et al.*, 2008; *Khain et al.*, 2008b].

[3] Aerosols transported across long distances, usually in discrete layers confined to narrow altitude regimes, can significantly alter the aerosol loading in remote locations. For instance, summer smoke plumes caused by boreal forest fires in Alaska and western Canada are frequently observed in both the boundary layer and free troposphere over the coastal northeast of the United States [*Wotawa and Trainer*, 2000; *Colarco et al.*, 2004; *Warneke et al.*, 2006; D. J. Miller et al., Evolution of a Canadian biomass burning aerosol smoke plume transported to the U.S. East Coast, submitted to *Journal of Geophysical Research*, 2011]. This occurs when a significant fraction of forest fire emissions are injected into the free troposphere [*Leung et al.*, 2007]. If synoptic conditions are favorable, the elevated plumes are transported eastward and entrained to the boundary layer, affecting mesoscale meteorology and air quality over the East Coast. Miller et al. (submitted manuscript, 2011) showed that carbonaceous aerosols (organic and black carbon) and sulfate aerosols are important components of forest fire plumes by synthesizing ground-based in situ and remote aerosol observations (e.g., photometer, lidar, Interagency Monitoring of Protected Visual Environments (IMPROVE), Environmental Protection Agency AIRNow), as well as analyzing satellite measurements (e.g., Moderate Resolution Imaging Spectroradiometer, Ozone Monitoring Instrument, Multiangle Imaging Spectroradiometer, Cloud-Aerosol Lidar and Infrared Pathfinder Satellite Observation, Atmospheric Infrared Sounder). The concentration ratio of black carbon to sulfate varies from about 1:5 to 1:12 at three IMPROVE sites over the northeastern United States during summer boreal forest fire episodes (Miller et al., submitted manuscript, 2011).

[4] During the summer of 2004, the International Consortium for Atmospheric Research on Transport and Transformation

[1]Scripps Institution of Oceanography, University of California, San Diego, La Jolla, California, USA.

0148-0227/12/2011JD016744

(ICARTT) coordinated several separate atmospheric field campaigns over North America to facilitate understanding of regional air quality and pollutant transport [*Fehsenfeld et al.*, 2006]. Within this time, wildfires in Alaska and western Canada burned 5.8 million hectares of boreal forest, an overall area much greater than the long-term annual average [*Stohl et al.*, 2006; *French et al.*, 2003; *Stocks et al.*, 2003]. Satellite and in situ observations showed that black carbon from these boreal wildfires was transported to Chebogue Point, Nova Scotia, about a week after the fire events. In addition, fire aerosols were detected both in the free troposphere (~8 km altitude) and in the boundary layer [*Duck et al.*, 2007]. Boreal forest fire plumes were also detected by Proton-Transfer-Reaction Mass Spectrometer aboard the NOAA WP-3 research aircraft [*de Gouw et al.*, 2006]. Also, the NOAA research vessel *Ronald H. Brown* situated in the Gulf of Maine detected aerosols using Proton-Transfer Ion-Trap Mass Spectrometry and online gas chromatography–mass spectrometer [*de Gouw et al.*, 2006; *Warneke et al.*, 2006].

[5] Adding to the complexity, aerosol plumes are also transported long distances in the stratosphere, frequently at altitudes between 10 and 20 km altitude [*Dean et al.*, 1994; *Ellrod*, 2004]. These volcanic aerosols are the main natural sources of sulfate aerosols [*Graf et al.*, 1997; *Allen et al.*, 2002]. The high injection height allows these plumes to sustain a long residence time and travel long distances. These aerosols impact climate globally by reducing the amount of solar radiation that reaches the ground and thus, lower the overall temperature in the troposphere [*Lamb*, 1970; *Dickinson*, 1996; *Robock*, 2000]. Some studies imply that volcanic aerosols alter the microphysics of cirrus clouds [*Jensen and Toon*, 1992; *Sassen et al.*, 1995].

[6] Numerical simulations and theoretical experiments focusing on strong, local aerosol emissions emphasize that the aerosol-induced precipitation response depends on both the convection regime and environmental conditions, such as atmospheric humidity [*Tao et al.*, 2007; *Khain et al.*, 2008b] and vertical wind shear [*Fan et al.*, 2009]. Several competing factors come into play. The aerosol-induced decrease in cloud droplet size slows the autoconversion of cloud droplets into raindrops ("aerosol second indirect effect") [*Albrecht*, 1989]. This precipitation suppression process is thought to dominate the overall aerosol effects on rainfall from shallow convection or continental clouds in a relatively dry environment [*Radke et al.*, 1989; *Rosenfeld*, 2000; *Khain et al.*, 2008b]. In contrast, for deep convection in a moist environment, aerosols have the capacity to invigorate the convection as less precipitation allows more cloud water to ascend to altitudes above the freezing level, leading to enhancement in upward heat transport and greater amounts of precipitation during the later stage of the cloud cycle [*Rosenfeld et al.*, 2008; *Wang*, 2005]. *Fan et al.* [2009] pointed out that vertical wind shear also plays a key role in regulating aerosol effects on isolated deep convective clouds, and it is shown that an increase in aerosol loading under strong wind shear leads to convection suppression, and vice versa. Note that the invigorating process only occurs when deep convective clouds develop in a moist environment with a warm cloud base (greater than ~15°C) [*Rosenfeld et al.*, 2008] and when ice-phase processes play a major role in rain production [*Molinié and Pontikis*, 1995; *Williams et al.*, 2002]. It would be interesting to explore whether the aforementioned long-distance transported aerosols, which normally represent weaker aerosol perturbations than those employed in studies that have focused on the impact of local emissions on convection and precipitation, also lead to a detectable precipitation suppression or enhancement signal.

[7] Explicit atmospheric simulations with online chemistry present an opportunity to explore the ways convective systems are impacted by aerosols of distant origin. The Weather Research and Forecasting model with Chemistry (WRF-Chem) [*Grell et al.*, 2005] makes for an ideal testbed because local and nonlocal aerosols are treated separately. Although previous WRF-Chem studies on aerosol-cloud interactions have been undertaken, they focus almost exclusively on the effects of locally emitted aerosols: *Fast et al.* [2006] predicted a 30 to 40 W m^{-2} aerosol radiative forcing because of local emissions in the vicinity of Houston, Texas. *Chapman et al.* [2009] explored the meteorological impact of local emissions above the surface layer of western Pennsylvania. Compared to the base case with local emissions from both surface and elevated sources, their simulations showed that excluding elevated point emissions results in optically thinner clouds and a 31% increase in domain-average total rainfall [*Chapman et al.*, 2009]. *Ntelekos et al.* [2009] emphasized that local emissions could lead to precipitation suppression or enhancement, depending on aerosol concentration and meteorological conditions.

[8] Highly simplified aerosol and trace—gas boundary conditions are commonly applied in regional modeling studies on aerosol-cloud interactions. Temporal-spatial invariant vertical profiles, representing either the mean conditions for the simulation period [*Winner et al.*, 1995; *Fast et al.*, 2006; *Gustafson et al.*, 2007] or typical clean conditions [*Grell et al.*, 2010; *Sessions et al.*, 2010], are used as chemical boundary conditions. Some recent studies [*Fast et al.*, 2009; *Pfister et al.*, 2011] use a coarse global chemical transport model, such as Model for Ozone and Related Tracers [*Horowitz et al.*, 2003], to provide boundary conditions for regional simulations. Although the time-dependent boundary conditions from the global chemical transport model are a big improvement over constant profiles, they still do not contain much of the detailed plume information due to the coarse spatial and temporal resolution of the global model.

[9] The following idealized study was designed to probe the uncertainties that are introduced by neglecting nonlocal aerosol plumes in previous explicit simulations of aerosol impacts on regional meteorology. WRF-Chem was applied to investigate the sensitivity of an explicitly simulated summertime convective system over the northeastern Unites States with the height of nonlocal aerosol plumes. Idealized aerosol plumes were added on the upstream lateral boundary of the modeled domain at three different altitudes, where long-range transported aerosols are often observed over this region during summertime. In accordance with observations from regional field campaigns like ICARTT, the plumes were made up of (1) a mixture of sulfate and black carbon, to represent boreal forest fire emissions; and (2) sulfate only, to represent volcanic aerosols. We then investigated

the impacts of these nonlocal plumes on the WRF-Chem simulated clouds, precipitation, and temperature.

2. WRF-Chem Model and Experimental Design

[10] WRF-Chem version 3.2 (V3.2) is applied in this study. Section 2.1 briefly describes the WRF-Chem model. Section 2.2 describes the model configuration, including domain setup and model physics. Section 2.3 lays out the design of the numerical experiments that structured this study.

2.1. WRF-Chem Model

[11] Weather Research and Forecasting model (WRF) [*Skamarock et al.*, 2008] is a fully compressible, nonhydrostatic, mesoscale model. The governing equations are written in flux form to conserve mass and dry entropy. WRF-Chem [*Grell et al.*, 2005] is the chemistry version of WRF. Trace gases and aerosols are simulated online with meteorological fields to allow explicit interaction between chemistry and dynamics.

[12] The WRF-Chem V3.2 has several gas-phase chemistry and aerosol treatments. In this study, the Regional Acid Deposition Model, version 2 [*Stockwell et al.*, 1990] gas-phase chemistry is used in combination with the Modal Aerosol Dynamics Model for Europe (MADE) [*Ackermann et al.*, 1998]/Secondary Organic Aerosol Model (SORGAM) [*Schell et al.*, 2001] aerosol module. Three lognormal-distributed modes (Aitken, accumulation and coarse modes), two of which are for submicrometer aerosols, are used in the MADE/SORGAM aerosol module to represent particle size distribution. The aerosol "direct effect" can be activated by transferring the prognostic aerosol optical properties (i.e., aerosol optical thickness, single-scattering albedo, and asymmetry parameters) to the Goddard shortwave radiation scheme [*Chou et al.*, 1998], where aerosol absorption and scattering of incoming solar radiation are calculated [*Fast et al.*, 2006]. (Note that the aerosol effect on longwave radiation is not included in this version of WRF-Chem).

[13] Aerosol "indirect effects," aerosol activation and resuspension, aqueous-phase chemistry, and particle scavenging are implemented in this version of WRF-Chem [*Chapman et al.*, 2009]. A prognostic cloud droplet number concentration is included in the modified, double-moment version of Lin microphysics (hereinafter referred as "double-moment Lin") [*Lin et al.*, 1983], whereby simulated aerosol particles can be activated to form cloud droplets. Aerosol activation is based on maximum supersaturation as calculated from explicitly resolved updraft velocities and aerosol properties [*Abdul-Razzak and Ghan*, 2002]. Cloud droplet number concentration and droplet size are linked to the autoconversion of cloud droplets to rain droplets [*Liu et al.*, 2005]. In this way, the aerosol "second indirect effect" is also implemented. Nevertheless, because aerosol-cloud-radiation interaction pathways described previously are currently only implemented for water clouds in this version of WRF-Chem, a cautious approach is prudent when simulating mixed-phase and ice clouds.

2.2. Model Configuration

[14] Three nested domains (Figure 1) with two-way nesting are configured with horizontal grid resolutions of 27, 9, and 3 km. The innermost domain (Figure 1, d3) covers most of the continental U.S. portion of the ICARTT field campaign study area. Each of the three domains employs 35 stretched vertical layers, with the top of the model extending to 100 mb ($\sim$16 km). Vertical spacing of the model cells increases with altitude, beginning with eight levels contained from the first kilometer to the surface to capture boundary layer processes.

[15] The model was integrated from 5 August 2004 00:00 UTC to 9 August 2004 00:00 UTC. During this time period, the remnants of tropical storm Bonnie [*Atlas et al.*, 2005] passed through the northeastern section of the outermost domain with a high pressure to the West (Figure 1, d1). The associated flow provided a coherent pathway to transport idealized plumes injected into the northern boundary of the outermost domain as a way to arrive at the innermost domain (Figure 1). A combined orographic and frontal lifting produced deep convection and precipitation within the innermost domain.

[16] Initial and lateral boundary conditions for the meteorological fields, as well as initial sea surface temperature, soil temperature, and soil moisture, were obtained from the National Centers for Environmental Prediction (NCEP) North American Regional Reanalysis (NARR) with a spatial resolution of 32 km and a temporal resolution of 3 hours.

[17] A vertical profile for each gas-phase and aerosol species, based on results from NOAA Aeronomy Lab Regional Oxidant Model (NALROM) [*Liu et al.*, 1996], was used to initialize the simulation. These profiles represented clean background midlatitude conditions in the Northern Hemisphere and were also used as chemical boundary conditions for the outermost domain in the base simulation. Details for modifying these background conditions to represent idealized long-range transported aerosol plumes are described in section 2.3. Lateral boundary conditions (meteorological conditions and chemical concentrations) for the interior domains (Figure 1, d2 and d3) were derived from the surrounding domains (Figure 1, d1 and d2).

[18] Anthropogenic emissions within all three domains were turned off to isolate the aerosol's effects from the prescribed nonlocal aerosol plumes. By excluding anthropogenic emissions and using idealized profiles that represent a clean environment for initial and boundary chemical conditions, the base simulation represents cleaner conditions than what is typical for the northeastern United States. For example, in the base case simulation, cloud condensation nucleus (CCN) concentration at 0.4% supersaturation is $\sim$160 cm^{-3} when averaged over the innermost domain. This concentration is within a range typically observed only in remote continental regions [*Andreae*, 2009]. In this respect, our idealized study was carried out in an environment with low particle concentration.

[19] Table 1 summarizes the configuration options for physical and chemical processes in the simulation. We applied the Grell 3D cumulus parameterization [*Grell and Devenyi*, 2002] solely for the two exterior domains. For the high-resolution (3 km) interior domain, WRF-Chem was allowed to explicitly resolve the convective eddies. Four-dimensional data assimilation (also called analysis nudging) was applied to the outermost domain using NARR to prevent the simulated synoptic-scale features from drifting. The aerosol direct and indirect effects were activated by turning on the aerosol-radiation interactions in the Goddard shortwave radiation

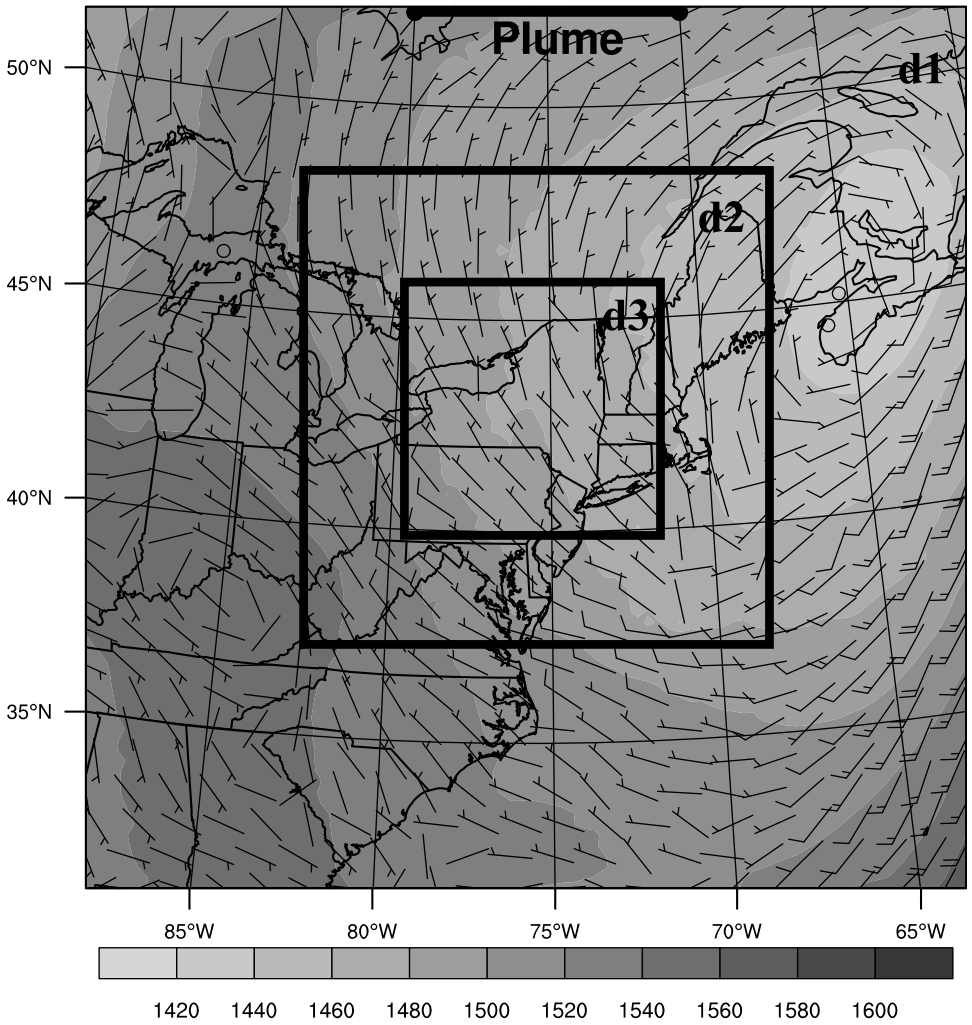

Figure 1. WRF-Chem domains overlaid with geopotential height (shaded, in meters) and wind vectors at 850 mb on 7 August 2004 18:00 UTC in CNTL no-plume simulation. Release location of aerosol plumes at low altitude, midaltitude, and high altitude are indicated by a thick line and "Plume" on the northern boundary of the outermost domain. Release heights of these aerosol plumes are listed in Table 2.

scheme and the aerosol-cloud-radiation interactions in the double-moment Lin microphysics. Feedback from the parameterized convection to radiation was turned on as well. By convention, the first two days of integration (model spin-up) was not analyzed. All analyses were based on simulation results from the interior domain with explicit convection (Figure 1, d3).

2.3. Experiment Design

[20] A suite of plume-height sensitivity tests was designed to probe the potential roles played by nonlocal aerosol plumes to influence a diurnal convective system occurring over northeastern New York during an ICARTT period.

[21] Plumes were introduced by modifying upstream aerosol boundary conditions of the outermost domain (Figure 1). The simulations were carried out with continuous aerosol fluxes at the northern boundary representing plumes of different compositions transported at three discrete altitudes ("low-altitude plume," "midaltitude plume," and "high-altitude plume"; Table 2). Vertical profiles for gas-phase species and aerosols obtained from the NALROM (section 2.2) were used as the chemical boundary conditions for the no-plume simulation (CNTL). For the plume cases, the chemical boundary conditions were set as a superposition of the idealized vertical profiles and prescribed aerosols

Table 1. Selected WRF-Chem Configuration Options[a]

Atmospheric Process	WRF-Chem Option
Microphysics	Double-moment Lin
Longwave radiation	RRTM [*Mlawer et al.*, 1997]
Shortwave radiation	Goddard [*Chou et al.*, 1998]
Surface layer	Monin-Obukhov [*Janjic*, 1996]
Land surface	Noah LSM [*Chen and Dudhia*, 2001]
Boundary layer	YSU [*Hong and Lim*, 2006]
Cumulus clouds	Grell 3D [*Grell and Devenyi*, 2002], domains 1 and 2 only
Aerosol-radiation interaction	On
Aqueous-phase chemistry	On
Aerosol-cloud-radiation interaction	On
Advection	Monotonic
Analysis nudging	Applied to the outermost domain only

[a]RRTM, Rapid Radiation Transfer Model; LSM, Land Surface Model; YSU, Yonsei University.

Table 2. Aerosol Boundary Conditions Over "Plume"[a]

Case	Height (km)	Sulfate (μg m^{-3})	Black Carbon (μg m^{-3})	Release Start Time
CNTL[b]				
Low	1.5–2.5	6	1	Initial
Mid	5.5–6.5	6	1	1 day after
High	11.5–12.5	20	0	1 day after

[a]Thick line on northern boundary of outermost domain shown in Figure 1.
[b]Idealized profile from NALROM (section 2.2).

(Table 2), which were added between 70°W and 80°W along the northern boundary of the outermost domain (Figure 1) at different altitudes. A mixture of sulfate (6 μg m^{-3}) and black carbon (1 μg m^{-3}) was applied to the low-altitude and midaltitude plume cases to represent forest fire plumes that were emitted from Alaska and western Canada and then transported to the northeastern United States in the lower and upper troposphere. A sulfate-only (20 μg m^{-3}) plume was added to the high-altitude plume case to represent a moderate volcanic plume in the lower stratosphere.

[22] The horizontal position of the injection zone was chosen based on results from offline simulations in which aerosol plumes were released in a series of zonal subregions along the northern boundary of the outermost domain. These tests (not shown) confirmed that plumes released between 70°W and 80°W along the northern boundary are propagated by large-scale flow associated with the midlatitude cyclone into the deep orographic convective zone within the interior domain with explicit convection. Also, plume injection times were staggered to offset for stronger winds as altitude increases (Table 2) so all three plumes would intercept the convective system at approximately the same time. In this fashion, the sensitivity of the convective system on the plume height could be explored in a consistent and controlled numerical environment.

3. Results

[23] Thermodynamic meteorology and precipitation from the base case simulation were compared with in situ observations and precipitation analysis, followed by analyses of the transport of nonlocal elevated aerosol plumes to the explicitly simulated convection in the innermost domain. Impacts of these nonlocal plumes on cloud properties, precipitation, and temperature associated with convection were then determined. Finally, we looked at the scavenging of plume particles because of the wet removal processes in the convective system.

3.1. Base Case Validation

[24] The CNTL no-plume simulation reproduced the thermodynamic meteorology realistically (Figure 2). Simulated 2 m temperature, 2 m relative humidity, and 10 m wind speed from the innermost domain with explicit convection are validated against hourly surface observations from Meteorological Aviation Reports available from approximately 50 stations. The closest model cell is identified for each station, with Figure 2 showing the averages of the three variables for all stations and the adjacent model cells. The base simulation reproduced the observed 2 m temperature throughout the simulation reasonably well (Figure 2a). The model performance in replicating the 2 m relative humidity was better during late morning and afternoon, when the temperature (relative humidity) was high (low), than during other times of the day. A dry bias (within 10%) existed during the night and early morning (Figure 2b). The model underpredicted daytime wind speed and overpredicted nighttime wind speed (Figure 2c). The simulated bias (within 1 m s^{-1}, Figure 2c) for the 10 m wind speed was reasonable, considering a cyclone was passing through the domain during the simulation period, and any imprecise prediction of its intensity, position, and timing may contribute to wind bias. Note that although local emissions were excluded from this base simulation, the results (2 m temperature, relative humidity and 10 m wind, etc.) from the CNTL no-plume case were in good agreement with those from a test case that includes local emissions based on the National Emission Inventory 2005 (NEI-05). This suggests that local emissions did not play a significant role in modifying the overall atmospheric conditions over this region for this specific case study. Thus, the model biases shown in Figure 2 are mostly attributed to either the model's internal problem or the driving reanalysis data, rather than the exclusion of local and nonlocal aerosols. In summary, the close correspondence of the modeled and measured time series suggests that the CNTL no-plume simulation adequately captured the regional thermodynamic meteorology within the innermost domain during the simulation period.

[25] Figure 3 demonstrates the space-time structure of the observed and simulated diurnal rainfall cycle during the first day of the 2 day simulation. Rainfall cycles on the subsequent day were similar. In the NCEP stage IV precipitation analysis [*Lin and Mitchell*, 2005], which is based on radar/gauge observations, rainfall was centered at 43.5°N and 74°W (Figure 3d), an area of complex terrain (Figure 3a)

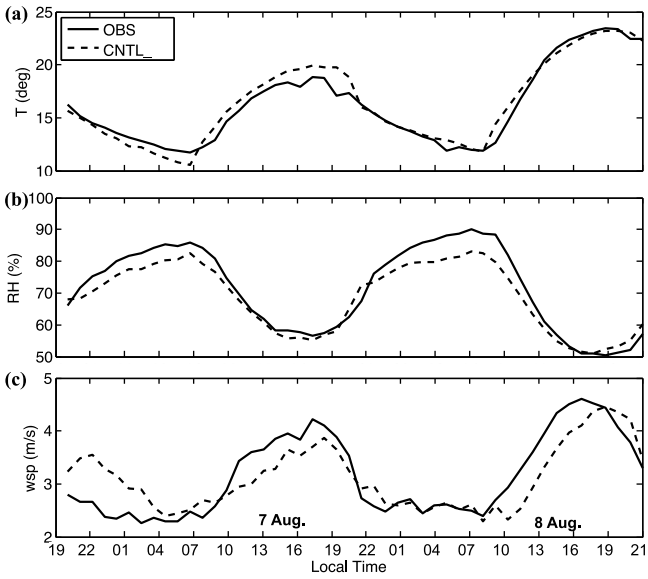

Figure 2. The CNTL no-plume case simulated (dashed line) and observed (solid line): (a) 2 m temperature, (b) 2 m relative humidity, and (c) 10 m wind speed averaged over all stations and adjacent model cells within the innermost model domain.

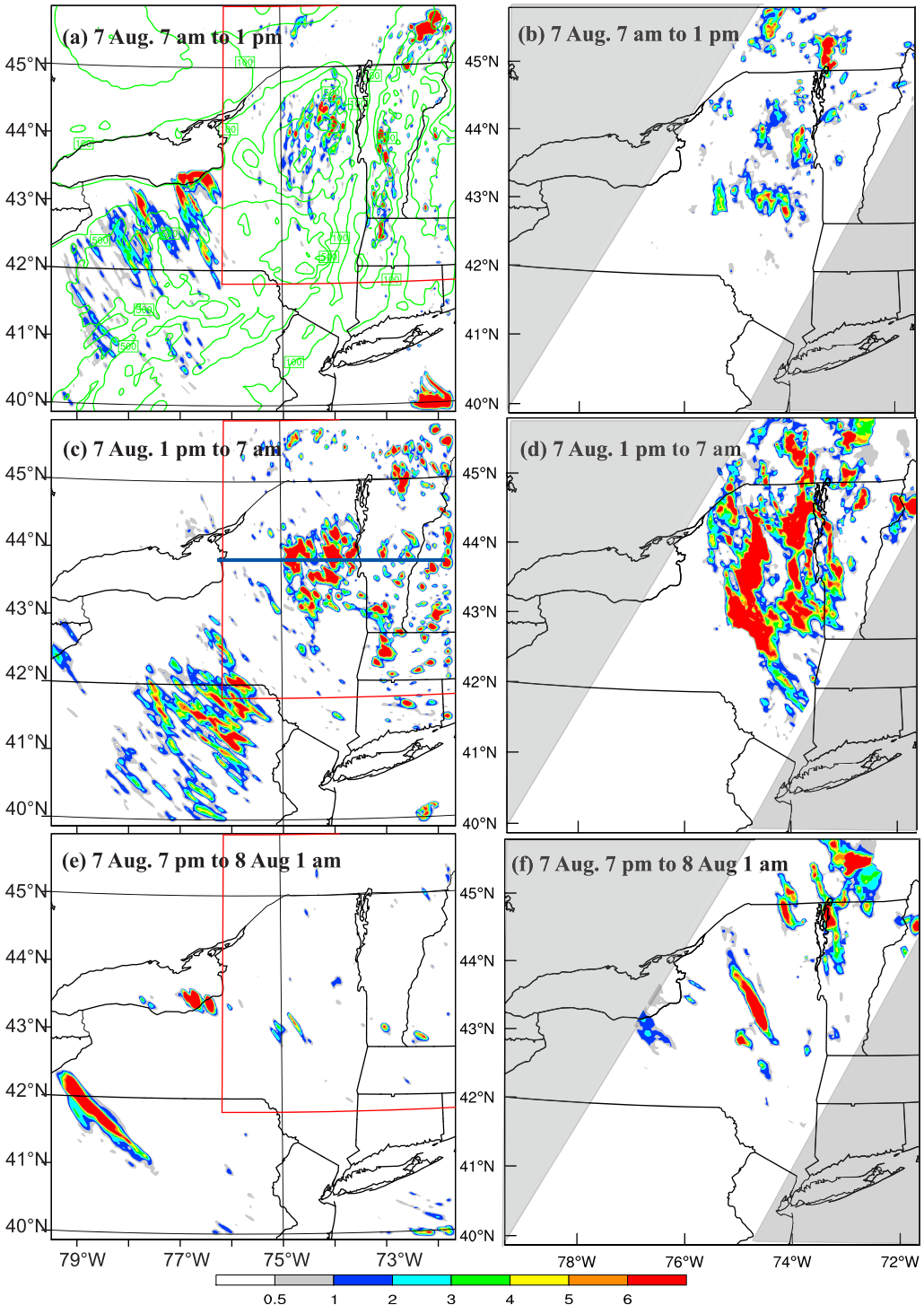

Figure 3. Accumulated precipitation (mm) from 7 August 07:00 to 13:00 LST from (a) the CNTL no-plume simulation, and (b) the NCEP stage IV 6 hourly precipitation analyses; from 7 August 13:00 to 19:00 LST from (c) the CNTL no-plume simulation, and (d) the NCEP stage IV precipitation analyses; and from 7 August 19:00 LST to 8 August 01:00 LST from (e) the CNTL no-plume simulation, and (f) the NCEP stage IV precipitation analyses. Terrain heights (green contours) are shown in Figure 3a with intervals of 200 m. The red box in Figures 3a, 3c, and 3e shows the AREA location. The portions grayed out in Figures 3b, 3d, and 3f indicate areas with missing observations. The blue line in Figure 3c indicates the location of the vertical cross section in Figures 7 and 9.

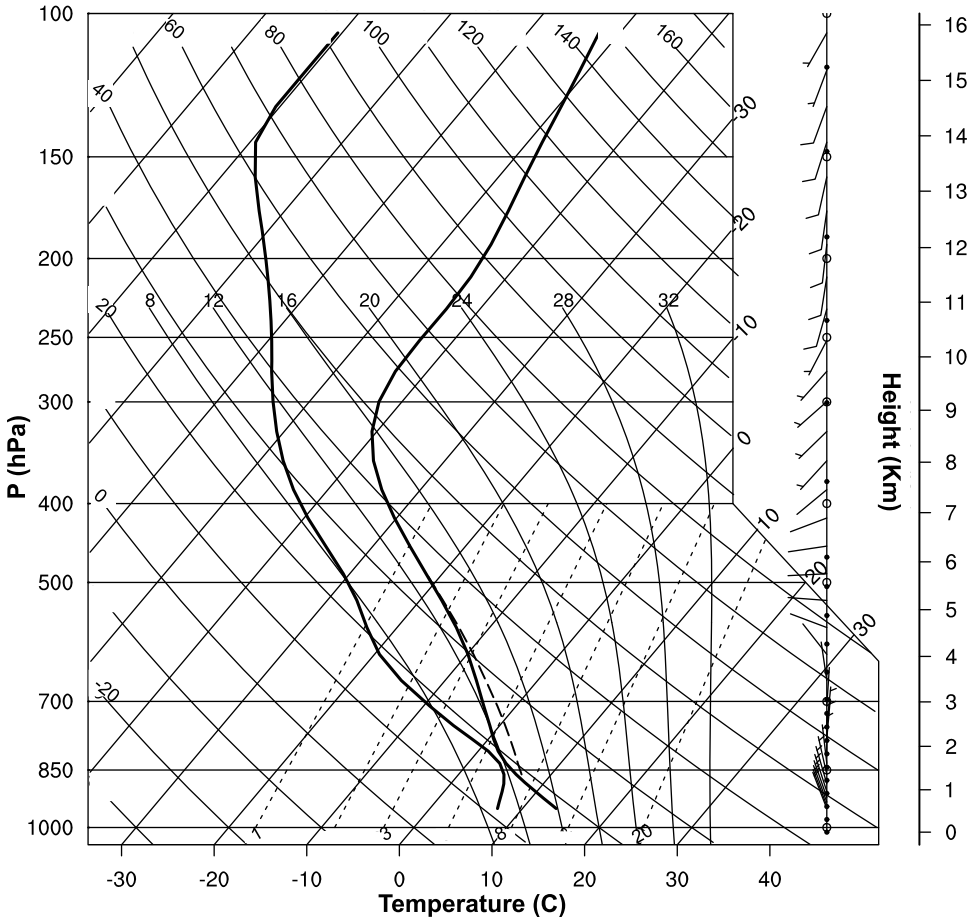

Figure 4. Skew-T diagram shows atmospheric stability characteristics of the innermost domain with explicit convection, averaged in space over the convection zone (AREA), and in time over the period of maximum rainfall (14:00–17:00 LST) on 7 August 2004. The dashed line shows the moist adiabatic buoyant ascent pathway for parcels raised to the lifting condensation level. The positive area between the dashed line and solid line for temperature indicates the ambient convective available potential energy.

well known to produce convection from morning chimney flows near mountain peaks [e.g., *Lu and Turco*, 1994]. Upscale enhancement of this orographic convection progressed into the afternoon and early evening with substantial afternoon rainfall (Figure 3d). After sunset, a few localized small-scale nocturnal systems also contributed some precipitation (Figure 3f). Figures 3a, 3c, and 3e show that in the interior domain with explicit convection, the CNTL no-plume simulation successfully captured a similar diurnal convection sequence in the vicinity of the topographic feature discussed previously.

[26] Some forecast biases were evident. For example, the modeled orographic afternoon convection east of Lake Erie was too weak compared to the NCEP stage IV data (Figure 3c vs. Figure 3d), and the simulated precipitation pattern was less organized with respect to observations. However, the overall progression of diurnal rainfall was realistic. In contrast, the simulation chronology to the Southwest did not agree well with the NCEP stage IV analysis. Nearby (42°N, 77°W), WRF-Chem produced unrealistic long-lived convective features, evidenced by rainfall streaks aligned with free tropospheric flow (cf. Figure 1). The rainfall streaks also showed up in the aforementioned test case that included local emissions based on NEI-05 emission inventory. This suggests that even though the simulation excluded local emissions, it was not responsible for this unrealistic convection. Analyses of variables over the region with unrealistic rainfall features (Figure 3) suggested that these convection features may be somewhat related to the modeled moisture over this region. For example, the model underestimated 2 m relative humidity when averaged over all stations within the modeled domain (Figure 2b), however, there were some overestimates (within 7%) when averaged only over stations in the region with these unrealistic rainfall features.

[27] To evaluate the effects of prescribed aerosol plumes on the diurnal orographic convection in the successfully simulated region east of Lake Erie, we focused on a subregion of interest in the northeast sector of the innermost domain, which we named "AREA" (Figures 3a, 3c, and 3e, red rectangle). The flow patterns shown in Figure 1 suggest that aerosol plumes prescribed between 70°W and 80°W along the northern boundary flow into AREA followed the northwesterly wind, whereas the unrealistically simulated rainfall streaks over Pennsylvania are located to the southwest of AREA (Figure 3c). Therefore, the parts of the

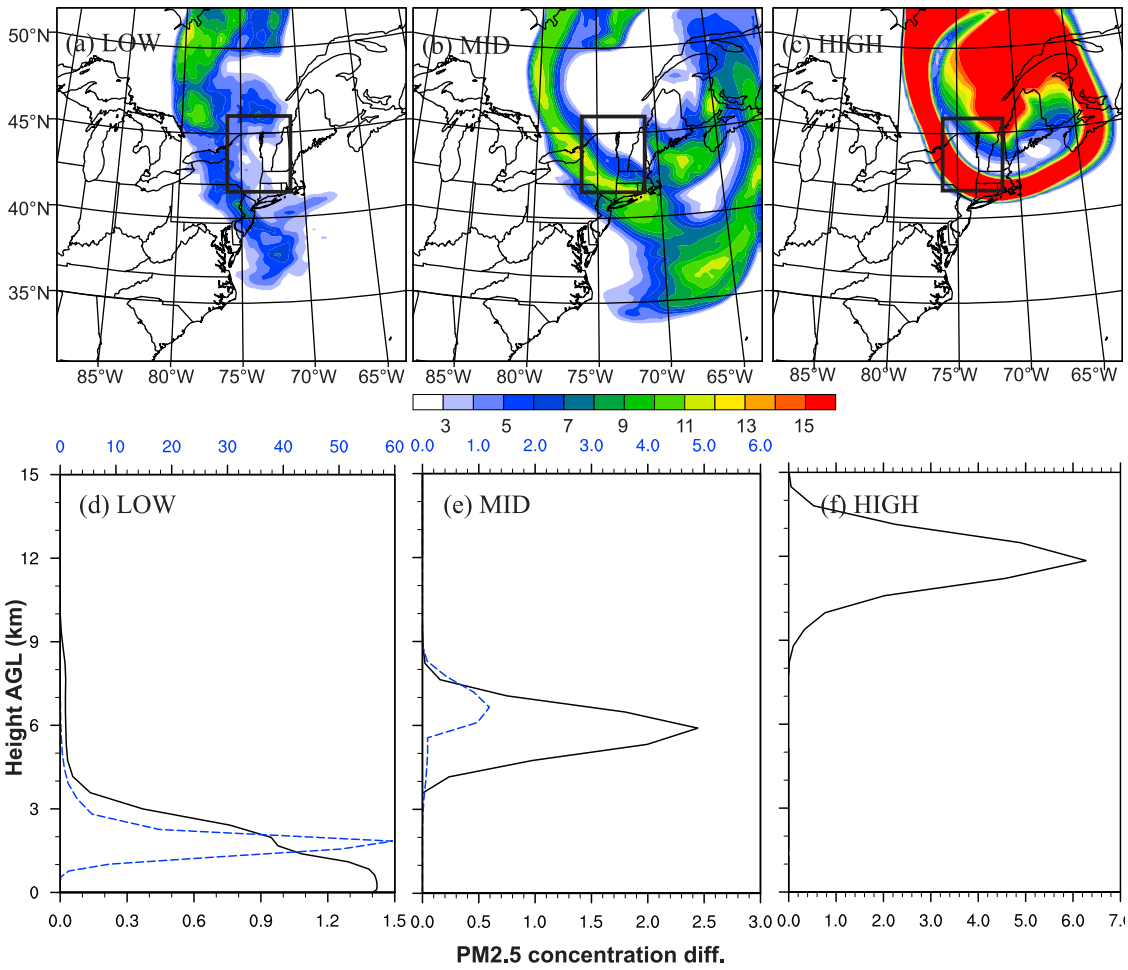

Figure 5. The outermost WRF-Chem domain simulated differences (relative to the CNTL no-plume case) in column-integrated $PM_{2.5}$ concentration (mg m^{-2}) for (a) low-altitude, (b) midaltitude, and (c) high-altitude plume cases on 8 August 2004 13:00 LST. The black rectangle in Figures 5a–5c shows the AREA location. (d–f) Vertical profile of AREA mean $PM_{2.5}$ concentration anomalies relative to the CNTL no-plume case (μg m^{-3}, solid black line) on 8 August 2004 13:00 LST are shown in Figures 5d–5f for low- altitude, midaltitude, and high-altitude plume cases, respectively. The CNTL no-plume case simulated cloud water and cloud ice-mixing ratio profile (mg kg^{-1}, dashed blue line) is shown in Figures 5d and 5e, respectively. Note that the *x* axes used in Figures 5d–5f are different; and the scale for cloud water mixing ratio in Figure 5d is an order of magnitude higher than that in Figure 5e for cloud ice.

aerosol plumes that flow into AREA do not interact with the unrealistic convection in the western portion of the domain. For this reason, the poor representation of rainfall over Pennsylvania (Figure 3) is unlikely to affect the reliability of the inferences on the effects of elevated aerosol plumes on the convective system over AREA. In the subsequent sensitivity analysis, we focused exclusively on this subregion.

[28] Figure 4 shows the dominant thermodynamic and stability characteristics averaged over AREA during the time of maximum precipitation (14:00–17:00 local standard time (LST)) on 7 August 2004. During this time, the 2 m relative humidity was around 60% (Figure 2b), indicating that convection develops in a relatively dry environment. Nevertheless, the atmosphere was conditionally unstable, providing lift through the subsaturated boundary layer. Potential buoyancy was available above a lifting condensation level at approximately 860 hPa, with maximum convective available potential energy (CAPE) values of 144 J. On average, convectively buoyant parcels are expected to reach maximum height at a neutral buoyancy level near 500 hPa. Because half the potential buoyancy is available above the 0° isotherm, ice-phase processes are involved.

3.2. Effects of Idealized Nonlocal Aerosol Plumes

3.2.1. Plume Transport to Explicit Convection Zone

[29] The prescribed nonlocal aerosol plumes successfully intercepted (horizontally) the convective AREA in all plume cases on 8 August 2004 13:00 LST (Figures 5a–5c). Low-level winds were generally weak with capricious wind directions caused by the impacts of surface friction and topography. In contrast, winds at higher altitudes were organized by the synoptic-scale system (a midlatitude cyclone in this case), providing a more conducive environment for the coherent transport of aerosol plumes to the

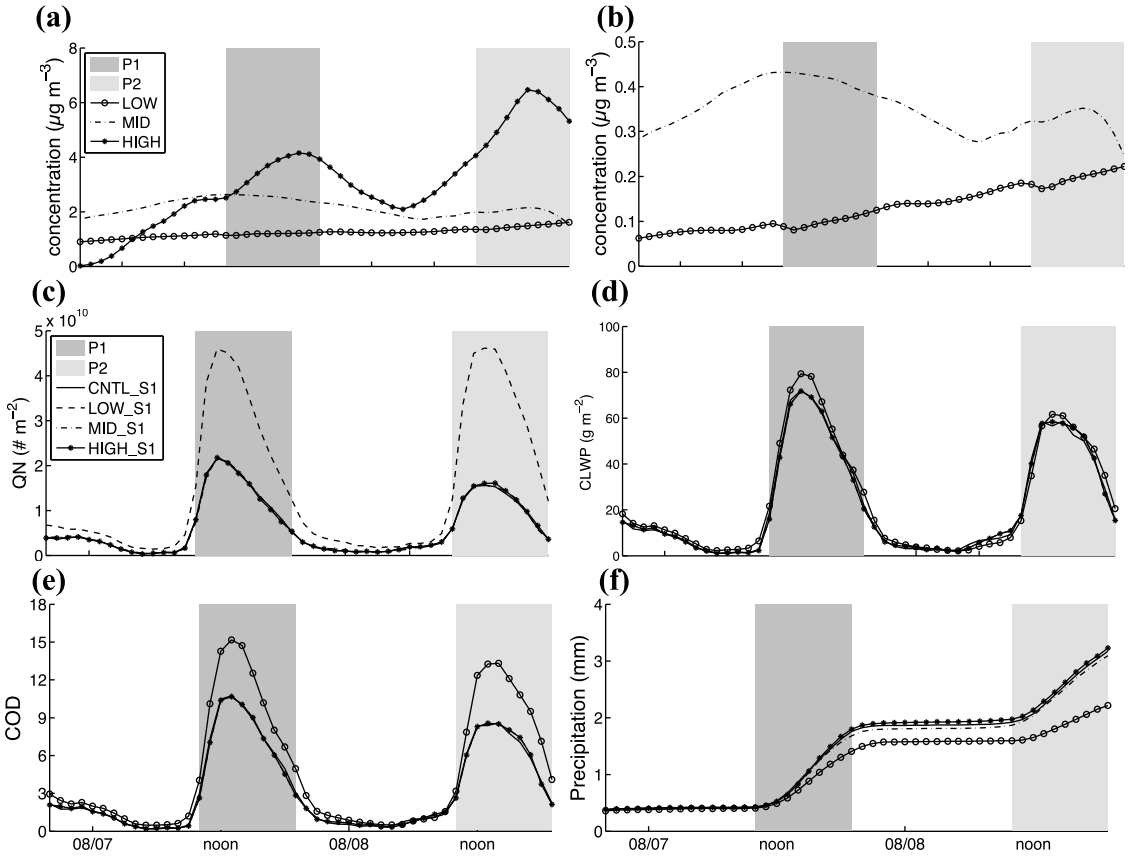

Figure 6. Time evolution of AREA mean (a) sulfate concentration at 12, 6, and 1 km altitude for high-altitude, midaltitude, and low-altitude plume cases, respectively, (b) black carbon concentration at 6 and 1 km altitude for mid- and low-altitude plume cases, respectively, (c) column-integrated cloud droplet number concentration (QN, in m^{-2}), (d) cloud liquid water path (CLWP, in g m^{-2}), (e) cloud optical depth (COD), and (f) accumulated precipitation (mm) from all four simulations. P1 and P2 are the two convection periods. Note that height ranges of 650, 580, and 260 m were used to average the concentrations at 12, 6, and 1 km, respectively.

innermost domain. As a result, the low-altitude plume (Figure 5a) was weak and disorganized, especially when transported over land, with a relatively short transport distance compared to plumes prescribed at midaltitude (Figure 5b) and high-altitude (Figure 5c).

[30] All three prescribed nonlocal plumes encountered the convective region with different horizontal structure at different altitudes (Figure 5). The CNTL no-plume case simulated cloud water (Figure 5d) and cloud ice-mixing ratios (Figure 5e) indicate a cloud base of about 1 km, with the cloud top extending to 9 km. Clouds in a water and ice phase existed below and above about 4 km, respectively. Low-altitude (Figure 5d) and midaltitude (Figure 5e) plumes intersected water and ice clouds over the AREA, respectively. The high-altitude plume existed above the cloud top (Figure 5f). Figure 5 illustrates that maximum aerosol concentrations within the AREA occurred at about 1, 6, and 12 km in the low-altitude, midaltitude, and high-altitude plume cases, respectively.

[31] By staggering the injections of nonlocal plumes, we were mostly successful in achieving their coincident arrival times at different altitudes into the convective AREA, as shown by the time evolution of AREA mean sulfate and black carbon concentrations at altitudes with maximum aerosol concentration (Figures 6a and 6b). Yet because wind speed and direction vary at different altitudes, the arrival times of the plumes at different heights are still slightly offset. However, as of 6 August 2004 19:00 LST, the aerosol plume in each sensitivity experiment was clearly present in the AREA simultaneously (Figures 6a and 6b).

3.2.2. Nonlocal Plume Interaction With Convective Clouds

[32] The simulations of AREA mean column-integrated cloud droplet number concentration, cloud liquid water path, cloud optical depth, and accumulated precipitation (Figures 6c–6f) illustrate the diurnal characteristics of this convective system. The following analysis focuses on the impacts of these nonlocal aerosol plumes on clouds over the AREA during the two plume-influenced convective intervals (Figure 6, shaded areas) from 10:00 to 19:00 LST on 7 and 8 August 2004 (hereinafter these convective time periods of interest are named P1 and P2, respectively).

[33] The low-altitude plume induced a substantial microphysical perturbation to the convective system, an almost threefold increase in the simulated daily maximum cloud droplet number with respect to the CNTL no-plume case (Figure 6c, shaded areas). However, this plume induced only a modest increase in the cloud liquid water path (Figure 6d).

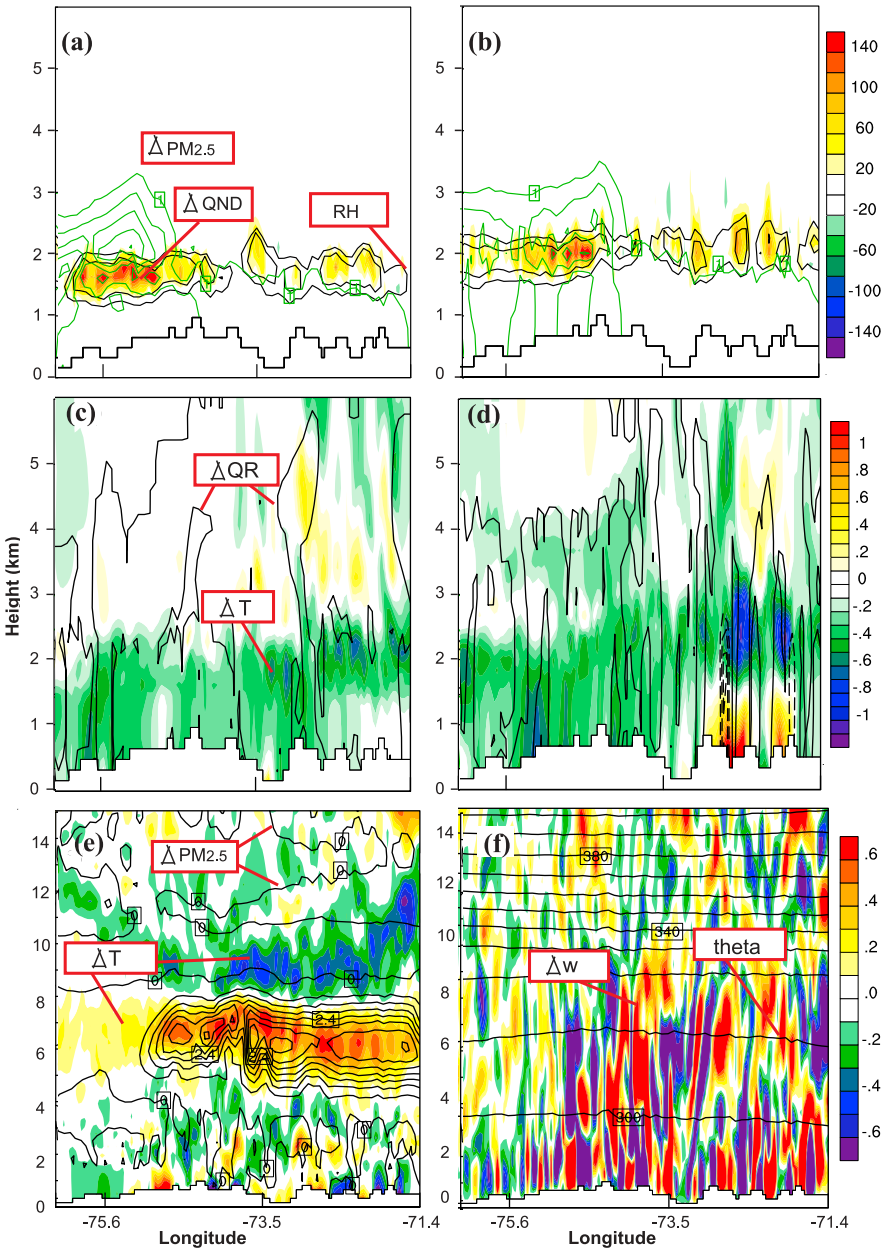

Figure 7. Differences (Δ) in low-altitude plume case relative to CNTL no-plume case for cloud droplet number concentration (QND, colors, in cm^{-3}) and $PM_{2.5}$ concentration (green contours, in $\mu g\ m^{-3}$ with interval of 0.5 $\mu g\ m^{-3}$) at (a) 10:00 LST, and (b) 13:00 LST 8 August 2004 along an east-west transect shown in Figure 3c. CNTL no-plume case simulated relative humidity (black contours) is superimposed at 90% and 95%. Differences in low-altitude plume case relative to CNTL no-plume case for temperature (T, colors, in K) and rainwater concentration (QR, black contours, in g m^{-3} with intervals of 0.1 g m^{-3}) along the same transect at (c) 10:00 LST, and (d) 13:00 LST 8 August 2004. Positive and negative QR differences are depicted by solid and dashed contours, respectively. Differences in midaltitude plume case relative to CNTL no-plume case for (e) temperature (T, colors, in K) and $PM_{2.5}$ concentration (black contours, in $\mu g\ m^{-3}$), and (f) vertical wind speed (w, colors, in dm s^{-1}) overlaid with CNTL no-plume case simulated potential temperature (theta, black contours, in K) at 7 August 2004 16:00 LST along the same transect. Contour interval for $PM_{2.5}$ concentration difference is 0.4 $\mu g\ m^{-3}$ in Figure 7e. Fields are meridionally averaged along a line that extends five grid points (15 km) into and out of the cross section.

More aerosols served as CCN, resulting in overall smaller cloud droplet size and larger surface area-to-volume ratios in the low-altitude plume case than those in the CNTL no-plume case. Thus, in the low-altitude plume case, cloud droplets evaporated more efficiently in the relatively dry environment. This may contribute to why the low-altitude plume and CNTL no-plume cases varied little in the cloud liquid water path. Compared to the CNTL no-plume case,

the low-altitude plume case simulated almost doubled daily maximum AREA mean cloud optical depth during both P1 and P2 (Figure 6e), which can be attributed to substantial increases in the cloud droplet number (Figure 6c). For the mid- and high-altitude plume cases, AREA mean cloud properties were almost identical to those for the CNTL no-plume case (Figures 6c–6e).

[34] The low-altitude plume produced the only substantial cloud-property response because it was the sole plume intersecting water clouds (Figure 5d), which then led to an increase in CCN concentration. As ice nuclei are not linked to the prognostic aerosol concentration in WRF-Chem V3.2, the midaltitude plume intersection of ice clouds (Figure 5e) did not affect the simulated cloud microphysical properties. Further discussion about changes to cloud properties and precipitation that may be induced by the midaltitude plume, if ice crystal formation is connected with prognostic aerosols, is provided in section 3.2.3.

[35] Response of cloud droplet number concentration to the low-altitude plume (Figures 7a and 7b) shows that the aerosol-induced increase of cloud droplet number concentration peaks at 120 cm^{-3}. Interestingly, although the aerosol plume extends vertically to approximately 3 km, especially to the west of 74°W where the $PM_{2.5}$ concentration increases to 3 $\mu g\ m^{-3}$, the boost in cloud droplet number concentration is confined to a thin layer between 1 and 2 km. This can be explained by considering the structure of the ambient relative humidity. Significant increases in cloud droplet number concentration only occur where the relative humidity is greater than 90% (Figures 7a and 7b), as aerosols can only be activated to form cloud droplets when the air parcel is supersaturated.

[36] The CNTL no-plume case represents a cleaner environment than the actual conditions that exist over this region (discussed in section 2.2). Previous studies [e.g., *Ramanathan et al.*, 2001; *Wang*, 2005] suggest that increases in CCN concentration generate a stronger response of cloud droplet number concentration in an environment with lower particle concentration. Thus, the impacts of the low-altitude plume on various cloud properties, as well as precipitation (discussed in section 3.2.3), may be overpredicted in this study relative to what would be expected with local emissions.

3.2.3. Nonlocal Plume Impact on Precipitation

[37] To investigate whether a precipitation suppression or enhancement signal can be detected by comparatively weak, nonlocal aerosol perturbations at the lateral boundary, we plotted time evolutions of AREA mean accumulated precipitation (Figure 6f). The low-altitude plume case produced considerably less precipitation (~30% reduction) compared to the CNTL no-plume case. In contrast, overall precipitation was minimally altered by aerosol plumes that intersected the ice clouds (midaltitude plume case) or that overlay the cloud-bearing layer (high-altitude plume case).

[38] The apparent reduction in precipitation is a consequence of the aerosol impact rather than changes in chronology of the simulated convection. Spatial distributions of the total surface precipitation during P1 and P2, for both the CNTL no-plume and the low-altitude plume cases (Figure 8), show that positioning of simulated rainfall is generally unchanged by the low-altitude plume. However, both the spatial extent and strength of precipitation over the AREA in the CNTL no-plume case (Figures 8a and 8c) are reduced considerably by the low-altitude plume (Figures 8b and 8d). This consistency suggests that the reduction in composite storm intensity (Figure 6f) is not an artifact of the repositioning of major storms relative to the averaging region.

[39] Is the mechanism supporting the significant precipitation response to the nonlocal low-altitude plume consistent with what has been synthesized by others in response to more extreme local emissions [e.g., *Cotton et al.*, 2007; *Khain et al.*, 2008a, 2008b; *Lim et al.*, 2011; *Zhang et al.*, 2007]? In this convective system, about 20% of the condensate mass is in the ice phase above 4 km (Figures 5d and 5e), rendering it active in this cloud system. However, this system developed in a drier environment (e.g., ~60% 2 m relative humidity during the convective periods, Figure 2b) than for the cases where convection invigoration was generally observed and simulated [*Rosenfeld et al.*, 2008; *Khain et al.*, 2008b]. The vertical wind shear associated with this convective system, which is calculated as the maximum minus the minimum wind component (U and V) within 7 km from the ground following the study of *Fan et al.* [2009], is ~5.3 and ~7.4 m s^{-1} for U-component and V-component, respectively. Therefore, this convective system is developed under relatively strong vertical wind shear, which is conducive for aerosol-induced convection suppression. Furthermore, according to *Rosenfeld et al.* [2008], our cloud base temperature (~10°C) is colder than the minimum cloud base temperature (~15°C) required for aerosol-induced invigoration of deep convective clouds to occur. These considerations suggest that for this simulated convection regime, an aerosol-induced precipitation suppression is more likely to occur. In this sense, our results showing suppression effects of a nonlocal low-altitude plume are consistent with mechanisms documented in other experiments that increase local aerosol emissions.

[40] Note that the modeling studies discussed previously [*Cotton et al.*, 2007; *Khain et al.*, 2008a, 2008b; *Lim et al.*, 2011; *Zhang et al.*, 2007; *Fan et al.*, 2009] are for single deep convective clouds, and the aerosol radiative effect is not considered. Yet for strongly absorbing aerosols, such as black carbon, the aerosol radiative effect can significantly impact convection and precipitation. For example, *Fan et al.* [2007] first showed aerosol-induced convection invigoration and precipitation enhancement when using a 2D cloud model but when *Fan et al.* [2008] used the same model and took into account the radiative effect of absorbing aerosols, an opposite overall aerosol effect on convection and precipitation was obtained for the same convective system. Both aerosol "indirect effect" and radiative effect are taken into account for simulations in this study. The absorbing aerosols in the low-altitude plume heats the atmosphere at the plume level, while simultaneously reducing sunlight from reaching the ground and resulting in a temperature reduction close to surface (figure not shown). These temperature variations caused by the aerosol radiative effect of the low-altitude plume tend to stabilize the atmosphere and consequently suppress the convection. Therefore, the ~30% precipitation reduction in the low-altitude plume case (compared to the CNTL no-plume case; Figure 6f) might be attributed to both the aerosol "indirect effect" and radiative effect.

[41] The interpretation of the simulated response to the midaltitude plume is necessarily limited by the lack of a

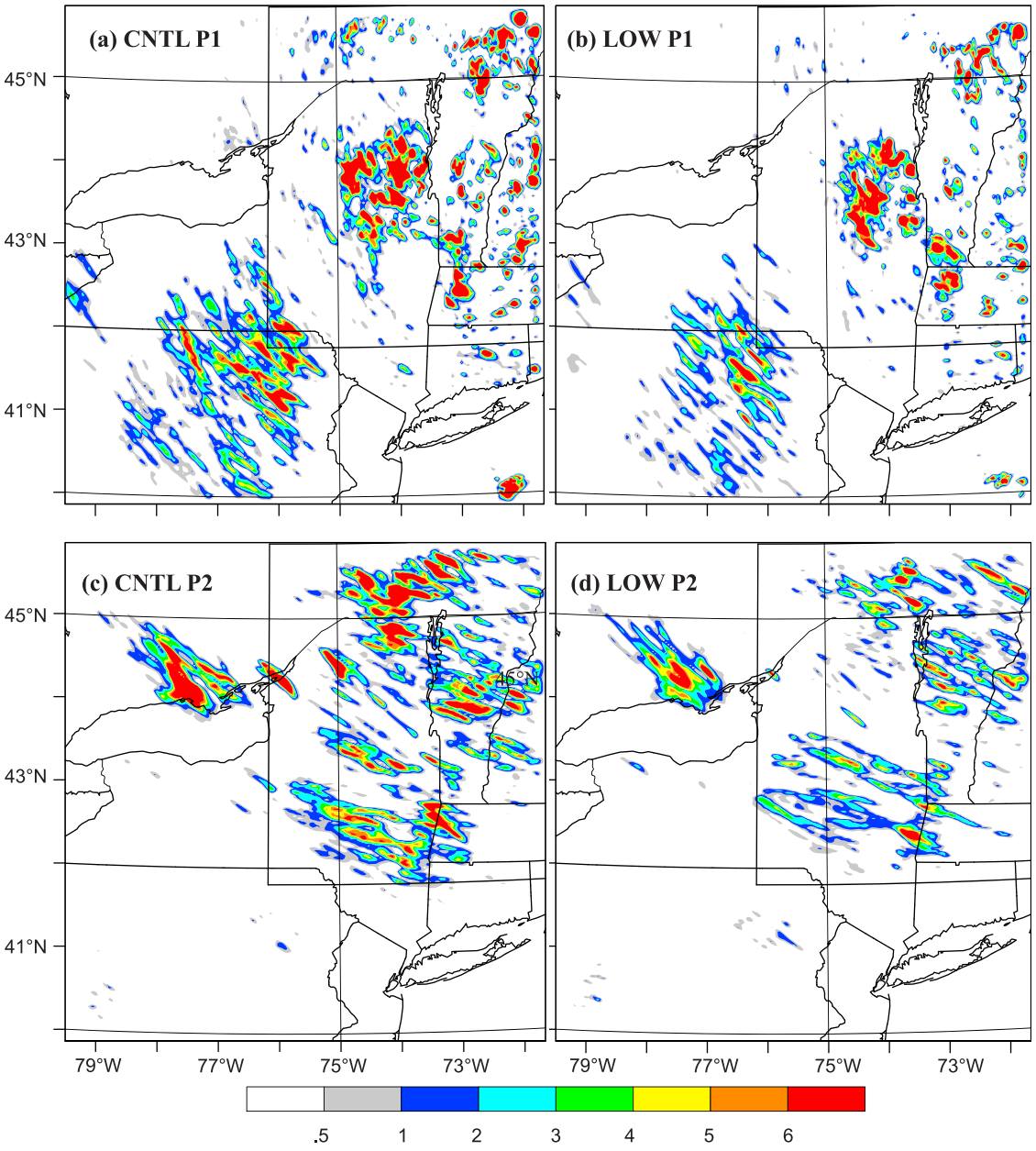

Figure 8. Accumulated precipitation (mm) during (a, b) P1 and (c, d) P2 from CNTL no-plume simulation (Figures 8a and 8c) and low-altitude plume simulation (Figures 8b and 8d). AREA is shown with black box in Figures 8a–8d.

prognostic treatment of ice nuclei in WRF-Chem V3.2 [*Chapman et al.*, 2009]. First, the lack of sensitivity of the convective system to the midaltitude plume is consistent with the study of *Fan et al.* [2010a], which shows that midtropospheric CCN have almost negligible effects on convection and cloud properties. Second, *Fan et al.* [2010a] and others [e.g., *Fridlind et al.*, 2004; *van den Heever et al.*, 2006; *Leroy et al.*, 2009] report that midtropospheric ice nuclei can modify the anvil properties of deep convective clouds and enhance glaciation of convective clouds in a humid environment. Although ice clouds were limited to only about 20% of the total cloud mass, the midtroposphere is relatively humid for the convective system in this case study (Figure 4). For example, the relative humidity averaged horizontally over AREA and vertically over 5 to 7 km altitudes is ~50% and ~35% during P1 and P2, respectively, which is close to the humid case discussed in the study of *Fan et al.* [2010a, 2010b]. Thus, if the ice nuclei formation is linked to prognostic aerosols in a future version of WRF-Chem, some modifications in convection and cloud properties caused by this midaltitude plume can be expected.

3.2.4. Nonlocal Plume Impact on Temperature

[42] The low-altitude plume resulted in an overall cooling below about 2.5 km (Figures 7c and 7d). This implies that the enhanced cooling below clouds because of optically thicker clouds in the low-altitude plume case (Figure 6e), which reflected more incoming sunlight back to space, took precedence over the heating effect of the absorbing black

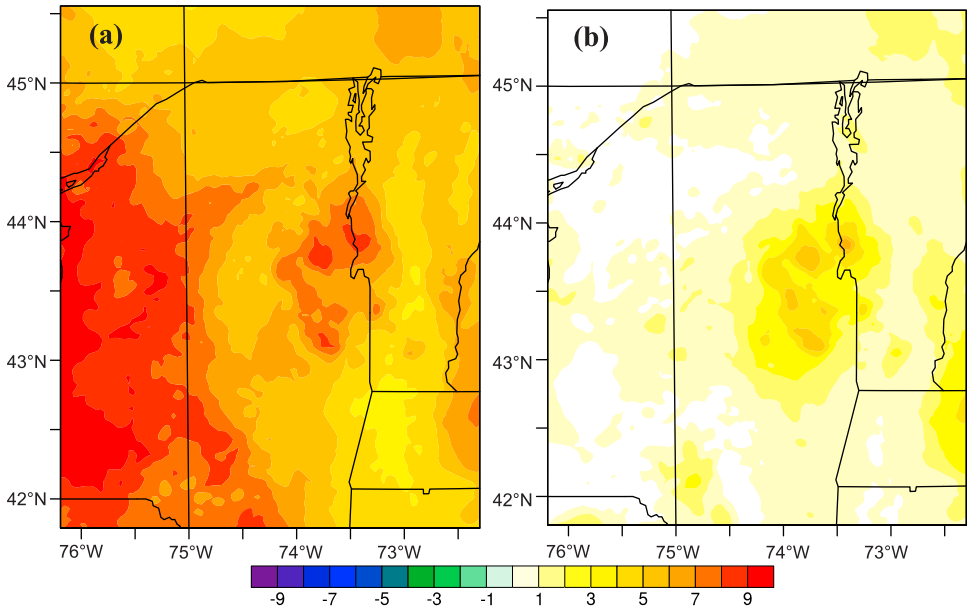

Figure 9. Spatial distribution (over AREA) of (a) column-integrated sulfate and black carbon concentration (mg m^{-2}) from LOW-NS plume case averaged over P1, 10:00 to 19:00 LST on 7 August 2004; and (b) differences of column-integrated sulfate and black carbon concentration for the LOW-NS case relative to the low-altitude plume case averaged over P1.

carbon in the plume. However, during periods of considerable variation in rainfall, temperature differences between the low-altitude plume and CNTL no-plume cases become more complicated (Figure 7d). In spite of an overall cooling below 2.5 km, warming occurs between 72°W and 73°W with a temperature increase up to 1 K close to surface, which approximately collocates to areas with rainfall suppression (Figure 7d, dashed contour lines). This suggests that the warming was caused by a decrease in evaporative cooling associated with the reduction of falling raindrops. The horizontal collocation (between 72°W and 73°W) of the ~1 K increase close to the surface and ~1 K decrease 2 to 3 km above the surface (Figure 7d) implies a potential modification to atmospheric stability and convection intensity, considering these temperature perturbations occur at altitudes with ambient environmental CAPE (Figure 4).

[43] The atmosphere's thermal response to the midaltitude plume was a heated layer in the plume arrival area, as well as a cooling layer above the aerosol layer (Figure 7e). As the midaltitude plume did not interact with water clouds (sections 3.2.2 and 3.2.3 discussion), the sunlight absorption of black carbon resulted in an obvious warming in the plume arrival areas (Figure 7e). This heated layer promoted stronger upward motion within and above the aerosol layer, compared to the CNTL no-plume case (Figure 7f). The intensified adiabatic cooling associated with stronger upward motion resulted in a distinct cooling layer atop the heated layer (Figure 7e) [*Chen et al.*, 2010]. Furthermore, the vertical gradient of θ (potential temperature) was much stronger above 8 km (Figure 7f), which may relate to the upper-level cyclone passing through, magnifying plume-induced adiabatic cooling above the aerosol layer. Note that aerosol-induced warming or cooling accumulates with time, so the pattern of the aforementioned cooling layer (Figure 7e) does not necessarily match the anomalies seen in the instantaneous upward motion (Figure 7f). Although the midaltitude plume considerably modified the atmospheric temperature within and above the aerosol layer, the impacts of this midaltitude plume on the instability of the atmosphere are small. The skew-T diagram averaged spatially over AREA and temporally over 14:00–17:00 LST on 7 August 2004 for the mid-altitude plume case (figure not shown) is similar to that for the CNTL no-plume case (Figure 4), and the corresponding CAPE is 140 and 144 J kg^{-1} for the mid-altitude plume case and CNTL no-plume case, respectively. The possible reason for such negligible changes on atmospheric instability can be that these temperature perturbations took place above ~5 km altitude (Figure 7e), which is more than where the maximum CAPE is reached (Figure 4). This also explains the almost unaltered cloud properties and convection intensity from the midaltitude plume case compared to the CNTL no-plume case (Figures 6c–6f).

[44] There was no evidence of thermal response to the sulfate-only high-altitude plume (not shown), despite the higher-aerosol concentration in the high-altitude plume case (20 μg m^{-3} pure sulfate) than that seen in the low-altitude and midaltitude plume cases (mix of 6 μg m^{-3} sulfate and 1 μg m^{-3} black carbon, Table 2). The multiple directions of scattering of sunlight by sulfate aerosols are likely the reason. The atmosphere's contrasting thermal response to mid- and high-altitude plumes emphasizes that the composition and optical properties of the plumes are important to aerosol-radiation interactions in regional WRF-Chem simulations.

3.2.5. Particle Scavenging of Convection on Aerosol Plumes

[45] Both in-cloud and below-cloud aerosol wet removal processes are treated in WRF-Chem V3.2 [*Chapman et al.*, 2009]. The removal of cloud-borne aerosols within clouds uses the first-order loss rate of cloud water. Again, this version of WRF-Chem does not treat aerosol removal within

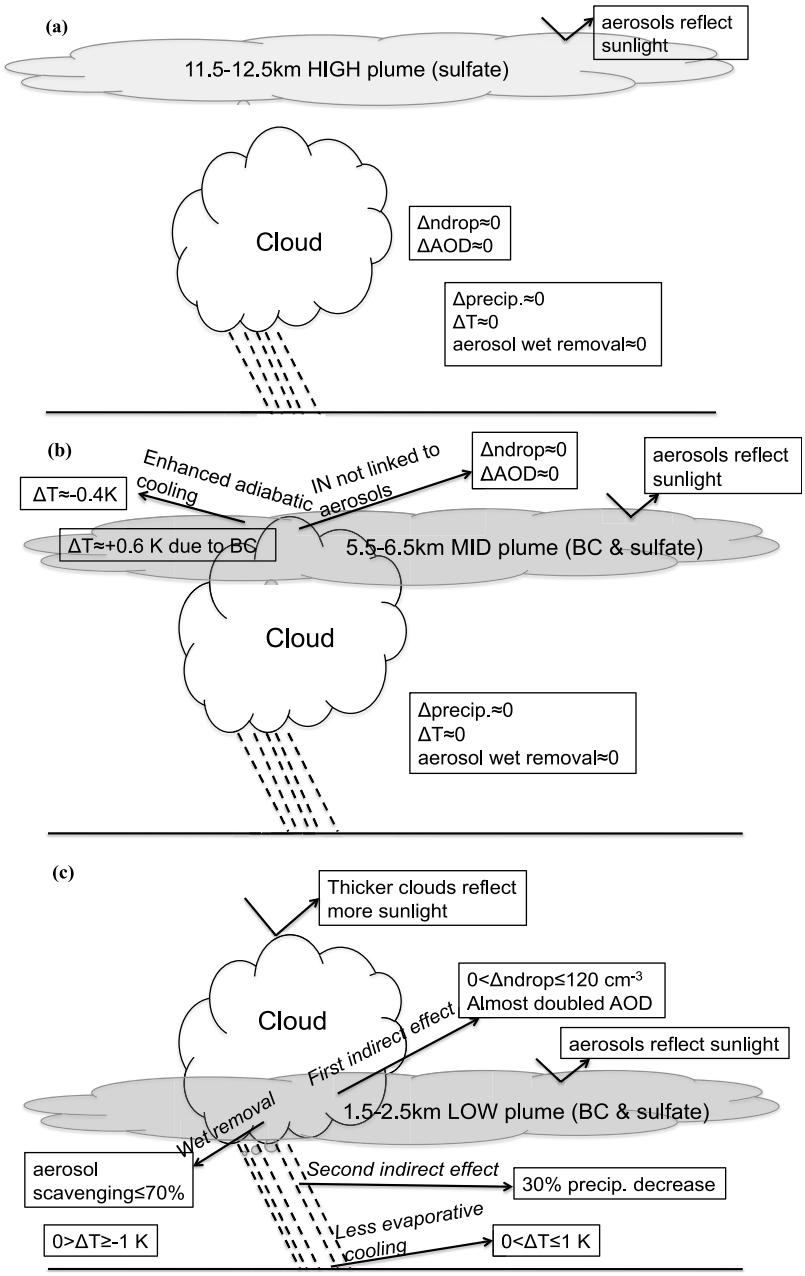

Figure 10. Impacts on clouds, precipitation, and temperature of aerosol plumes transported at (a) high altitude, (b) midaltitude, and (c) low altitude. "AOD" indicates cloud optical depth, "ndrop" indicates cloud droplet number concentration, and "IN" indicates ice nuclei.

ice clouds. On the basis of the previous discussions, aerosol scavenging is expected to occur only in the low-altitude plume, which existed within and below water clouds over the AREA. To examine the scavenging impact of the convective system on the low-altitude plume, a sensitivity simulation, named LOW-NS, was conducted using the same configuration as that for the low-altitude plume case, except both in-cloud and below-cloud scavenging of aerosols were turned off in double-moment Lin microphysics.

[46] The difference in aerosol mass from the LOW-NS plume simulation relative to that from the low-plume simulation yields the aerosol mass removed by the scavenging processes. Figure 9 illustrates the column-integrated sulfate and black carbon mass temporally averaged over P1 from the LOW-NS simulation (Figure 9a), as well as the sulfate and black carbon mass removed by scavenging processes during that period over the AREA (Figure 9b). By comparing Figures 9a and 9b, the fraction of plume aerosols removed by clouds and precipitation can be as high as 70% over regions where deep convection and precipitation occur (Figure 8b). However, the convection is also altered considerably in the nonscavenging case (LOW-NS) as compared to the case with it (low-altitude plume case). The exclusion of aerosol scavenging in the LOW-NS

nonscavenging case results in higher concentration of aerosols in this simulation compared to the low-altitude plume (with scavenging) case. This leads to more cloud droplets in the LOW-NS nonscavenging case than in the low-altitude plume case (~20% increase in the column-integrated cloud droplet number concentration during the convective periods), and consequently smaller droplet sizes in the LOW-NS case as the cloud liquid water path is almost identical in the two simulations. The smaller cloud droplet sizes slow the autoconversion from cloud droplets to rain droplets in Lin microphysics, leading to remarkable reductions in the convection intensity (total precipitation is reduced by ~50% in the LOW-NS nonscavenging case compared to the low-altitude plume case). More than 95% of the aerosols in the LOW-NS plume were in accumulation mode over the AREA, although equal concentrations were originally prescribed for aerosols in Aitken and accumulation modes along the upstream boundary (e.g., 3 and 0.5 μg m^{-3} were assigned to sulfate and black carbon, respectively, in each mode). In this case, most of the aerosols were converted to accumulation mode by coagulation and/or collision before being transported over the AREA. Therefore, particle scavenging mostly arose from aerosols in the accumulation mode in our case study.

[47] Interactions of nonlocal aerosol plumes with convection, precipitation, and temperature have proven rather complicated, particularly in the low-altitude plume case. Figure 10 provides a summary for the three plume cases to clarify the simulated responses to each as discussed in this section.

4. Conclusions and Discussion

[48] In this idealized case study, the upstream lateral boundary of the outermost WRF-Chem domain was modified to introduce idealized nonlocal aerosol plumes at three discrete altitudes (low, mid, and high) to evaluate the uncertainties introduced by excluding nonlocal, elevated aerosol plumes in conventional regional aerosol-climate sensitivity simulations.

[49] After transport to the convection region, the low-altitude and midaltitude plumes intersected water and ice segments of the cloud system, respectively. The high-altitude plume arrived well above the cloud-bearing layer. A significant amount of aerosols in the low-altitude plume were activated to form cloud droplets. As a result, compared with the CNTL no-plume simulation, the low-altitude plume case predicted optically thicker clouds (almost double the daily maximum depth), along with a small increase in the cloud liquid water path. Furthermore, the low-altitude plume demonstrated a significant precipitation response (~30% reduction in 2 day accumulated precipitation over the CNTL no-plume case), which is equal in magnitude to the rainfall modification projected from simulations that excluded all local, above-surface emissions [*Chapman et al.*, 2009]. The mechanism behind the precipitation suppression response of this simulated convection to the nonlocal low-altitude forest fire plume is qualitatively similar to behavior observed in experiments with enhanced local emissions.

[50] This suggests that neglecting lateral inflow plumes can indeed represent a significant omission in regional aerosol-climate simulations for areas impacted by the transport of substantial low-altitude plumes. In contrast, the midaltitude and high-altitude plume cases showed negligible sensitivity, emphasizing this potential source of error depends on the relative height of plumes transported from outside the modeled domain, as well as on how or where the plumes intersect the convective system. The insensitivity reflects the small cooling impact from the overlying high-altitude and mid-altitude plumes at this late stage of the convection, as opposed to the significant impact of the low-altitude plume on cloud droplet number.

[51] Results showing negligible sensitivity in the mid-altitude plume case should be treated with caution, as this plume intersected the ice phase of the cloud system, and the ice crystal formation is not linked to prognostic aerosols in the model. Although only ~20% of the cloud condensate existed in ice form in the simulated convective system, the atmosphere is relatively humid at the midaltitude plume arrival heights in this study, which is favorable for the activation of midtropospheric ice nuclei [*Fan et al.*, 2010a]. Therefore, the midaltitude plume might lead to some modifications in cloud properties, such as cloud anvils and convection intensity if ice microphysics were simulated explicitly.

[52] An increase in cloud albedo in the low-altitude plume case led to an overall temperature decrease below about 2.5 km, despite the heating effect of black carbon. The temperature modification of the low-altitude plume was more complicated for areas with considerable rainfall suppression because of reduced evaporative cooling of rain droplets. The sunlight absorption of the black carbon in the midaltitude plume resulted in a layer of increased temperature (up to 0.6 K). Atop this warm layer was a cool layer, the outcome of adiabatic cooling associated with an enhanced upward motion. However, most temperature perturbations in the midaltitude plume occurred above the ambient environmental CAPE; thus, their impact on convection was negligible. The sulfate-only plume in the high-altitude plume case did not induce apparent temperature changes at either the aerosol layer or the surface, suggesting that a moderate volcanic plume is likely to result in only minimal surface cooling within a short time period (3 days in this study).

[53] In all, this idealized study showed that when nonlocal aerosol plumes flowing laterally into a WRF-Chem domain are introduced at certain altitudes, they confer a detectible and significant effect on convection and surface precipitation, not unlike that observed or simulated to occur in experiments with enhanced local emissions. For the summertime orographic convection over northeastern United States analyzed here, the forest fire plume from Alaska and western Canada suppressed precipitation when synoptic flows brought the plume to the boundary layer during long-range transport. Applying the same aerosol composition, a 4 km difference in the plume's vertical position along the upstream lateral boundary (low-altitude vs. midaltitude plume) led to considerably different impacts on precipitation (30% reduction vs. no detectable signal). Although the detailed response is dependent on the convection regime, this study emphasizes the importance of vertical positioning and composition of nonlocal aerosol plumes at model lateral boundaries in regional climate simulations with explicit convection.

[54] **Acknowledgments.** This study is funded by the Department of Energy (DOE) grant DE-SC0002003. For discussions related to this study, we thank Song-You Hong of Yonsei University; Shu-Hua Chen of the University of California, Davis; and Gabe Kooperman and Richard

Somerville of Scripps Institution of Oceanography. Our gratitude also goes to Queen Bee at Louisiana Optical Network Initiative and Triton Resources at San Diego Supercomputer Center, which provided computer clusters for the model simulations. We are also grateful to three anonymous reviewers for providing constructive comments, which improved the article.

References

Abdul-Razzak, H., and S. J. Ghan (2002), A parameterization of aerosol activation: 3. Sectional representation, *J. Geophys. Res.*, *107*(D3), 4026, doi:10.1029/2001JD000483.

Ackermann, I. J., H. Hass, M. Memmesheimer, A. Ebel, F. S. Binkowski, and U. Shankar (1998), Modal aerosol dynamics model for Europe: Development and first applications, *Atmos. Environ.*, *32*(17), 2981–2999, doi:10.1016/S1352-2310(98)00006-5.

Albrecht, B. A. (1989), Aerosols, cloud microphysics, and fractional cloudiness, *Science*, *245*, 1227–1230, doi:10.1126/science.245.4923.1227.

Allen, A. G., C. Oppenheimer, M. Ferm, P. J. Baxter, L. A. Horrocks, B. Galle, A. J. S. McGonigle, and H. J. Duffell (2002), Primary sulfate aerosol and associated emissions from Masaya Volcano, Nicaragua, *J. Geophys. Res.*, *107*(D23), 4682, doi:10.1029/2002JD002120.

Andreae, M. O. (2009), Correlation between cloud condensation nuclei concentration and aerosol optical thickness in remote and polluted regions, *Atmos. Chem. Phys.*, *9*, 543–556, doi:10.5194/acp-9-543-2009.

Atlas, R., O. Reale, B.-W. Shen, S.-J. Lin, J.-D. Chern, W. Putman, T. Lee, K.-S. Yeh, M. Bosilovich, and J. Radakovich (2005), Hurricane forecasting with the high-resolution NASA finite volume general circulation model, *Geophys. Res. Lett.*, *32*, L03807, doi:10.1029/2004GL021513.

Chapman, E. G., W. I. Gustafson Jr., R. C. Easter, J. C. Barnard, S. J. Ghan, M. S. Pekour, and J. D. Fast (2009), Coupling aerosol-cloud-radiative processes in the WRF-Chem model: Investigating the radiative impact of elevated point sources, *Atmos. Chem. Phys.*, *9*, 945–964, doi:10.5194/acp-9-945-2009.

Chen, F., and J. Dudhia (2001), Coupling an advanced land-surface/hydrology model with the Penn State/NCAR MM5 modeling system. Part I: Model description and implementation, *Mon. Weather Rev.*, *129*, 569–585, doi:10.1175/1520-0493(2001)129<0569:CAALSH>2.0.CO;2.

Chen, S.-H., S.-H. Wang, and M. Waylonis (2010), Modification of Saharan air layer and environmental shear over the eastern Atlantic Ocean by dust-radiation effects, *J. Geophys. Res.*, *115*, D21202, doi:10.1029/2010JD014158.

Chou, M. D., M. J. Suarez, C. H. Ho, M. M. H. Yan, and K. T. Lee (1998), Parameterizations for cloud overlapping and shortwave single-scattering properties for use in general circulation and cloud ensemble models, *J. Clim.*, *11*, 202–214, doi:10.1175/1520-0442(1998)011<0202:PFCOAS>2.0.CO;2.

Colarco, P. R., M. R. Schoeberl, B. G. Doddridge, L. T. Marufu, O. Torres, and E. J. Welton (2004), Transport of smoke from Canadian forest fires to the surface near Washington, D. C.: Injection height, entrainment, and optical properties, *J. Geophys. Res.*, *109*, D06203, doi:10.1029/2003JD004248.

Cotton, W. R., H. Zhang, G. M. McFarquhar, and S. M. Saleeby (2007), Should we consider polluting hurricanes to reduce their intensity?, *J. Weather Modif.*, *39*, 70–73.

Dean, K., S. A. Bowling, and G. Shaw (1994), Satellite analyses of movement and characteristics of the Redoubt Volcano plume, January 8, 1990, *J. Volcanol. Geotherm. Res.*, *62*, 339–352, doi:10.1016/0377-0273(94)90040-X.

de Gouw, J. A., et al. (2006), Volatile organic compounds composition of merged and aged forest fire plumes from Alaska and western Canada, *J. Geophys. Res.*, *111*, D10303, doi:10.1029/2005JD006175.

Dickinson, R. E. (1996), Climate engineering. A review of aerosol approaches to changing the global energy balance, *Clim. Change*, *33*, 279–290, doi:10.1007/BF00142576.

Duck, T. J., et al. (2007), Transport of forest fire emissions from Alaska and the Yukon Territory to Nova Scotia during summer 2004, *J. Geophys. Res.*, *112*, D10S44, doi:10.1029/2006JD007716.

Ellrod, G. P. (2004), Impact on volcanic ash detection caused by the loss of the 12.0 lm "Split Window" band on GOES Imagers, *J. Volcanol. Geotherm. Res.*, *135*(1–2), 91–103, doi:10.1016/j.jvolgeores.2003.12.009.

Fan, J., R. Zhang, G. Li, and W.-K. Tao (2007), Effects of aerosols and relative humidity on cumulus clouds, *J. Geophys. Res.*, *112*, D14204, doi:10.1029/2006JD008136.

Fan, J., R. Zhang, W.-K. Tao, and K. I. Mohr (2008), Effects of aerosol optical properties on deep convective clouds and radiative forcing, *J. Geophys. Res.*, *113*, D08209, doi:10.1029/2007JD009257.

Fan, J., T. Yuan, J. M. Comstock, S. Ghan, A. Khain, L. R. Leung, Z. Li, V. J. Martins, and M. Ovchinnikov (2009), Dominant role by vertical wind shear in regulating aerosol effects on deep convective clouds, *J. Geophys. Res.*, *114*, D22206, doi:10.1029/2009JD012352.

Fan, J., J. M. Comstock, and M. Ovchinnikov (2010a), The cloud condensation nuclei and ice nuclei effects on tropical anvil characteristics and water vapor of the tropical tropopause layer, *Environ. Res. Lett.*, *5*(4), 044005, doi:10.1088/1748-9326/5/4/044005.

Fan, J., J. M. Comstock, M. Ovchinnikov, S. A. McFarlane, G. McFarquhar, and G. Allen (2010b), Tropical anvil characteristics and water vapor of the tropical tropopause layer: Impact of heterogeneous and homogeneous freezing parameterizations, *J. Geophys. Res.*, *115*, D12201, doi:10.1029/2009JD012696.

Fast, J. D., W. I. Gustafson Jr., R. C. Easter, R. A. Zaveri, J. C. Barnard, E. G. Chapman, G. A. Grell, and S. E. Peckham (2006), Evolution of ozone, particulates and aerosol direct radiative forcing in the vicinity of Houston using a fully coupled meteorology-chemistry-aerosol model, *J. Geophys. Res.*, *111*, D21305, doi:10.1029/2005JD006721.

Fast, J. D., et al. (2009), Evaluating simulated primary anthropogenic and biomass burning organic aerosols during MILAGRO: Implications for assessing treatments of secondary organic aerosols, *Atmos. Chem. Phys.*, *9*, 6191–6215, doi:10.5194/acp-9-6191-2009.

Fehsenfeld, F. C., et al. (2006), International consortium for atmospheric research on transport and transformation (ICARTT): North America to Europe—Overview of the 2004 summer field study, *J. Geophys. Res.*, *111*, D23S01, doi:10.1029/2006JD007829.

French, N. H. F., E. S. Kasischke, and D. G. Williams (2003), Variability in the emission of carbon-based trace gases from wildfire in the Alaskan boreal forest, *J. Geophys. Res.*, *108*(D1), 8151, doi:10.1029/2001JD000480.

Fridlind, A. M., et al. (2004), Evidence for the predominance of mid-tropospheric aerosols as subtropical anvil cloud nuclei, *Science*, *304*, 718–722, doi:10.1126/science.1094947.

Giorgi, F., X. Bi, and Y. Qian (2002), Direct radiative forcing and regional climatic effects of anthropogenic aerosols over East Asia: A regional coupled climate-chemistry/aerosol model study, *J. Geophys. Res.*, *107*(D20), 4439, doi:10.1029/2001JD001066.

Giorgi, F., X. Q. Bi, and Y. Qian (2003), Indirect vs. direct effects of anthropogenic sulfate on the climate of East Asia as simulated with a regional coupled climate-chemistry/aerosol model, *Clim. Change*, *58*, 345–376, doi:10.1023/A:1023946010350.

Graf, H.-F., J. Feichter, and B. Langmann (1997), Volcanic sulfur emissions: Estimates of source strength and its contribution to the global sulfate distribution, *J. Geophys. Res.*, *102*(D9), 10,727–10,738, doi:10.1029/96JD03265.

Grell, G. A., and D. Devenyi (2002), A generalized approach to parameterizing convection combining ensemble and data assimilation techniques, *Geophys. Res. Lett.*, *29*(14), 1693, doi:10.1029/2002GL015311.

Grell, G. A., S. E. Peckham, R. Schmitz, S. A. McKenn, G. Frost, W. C. Skamarock, and B. Eder (2005), Fully coupled "online" chemistry within the WRF model, *Atmos. Environ.*, *39*, 6957–6975, doi:10.1016/j.atmosenv.2005.04.027.

Grell, G., S. R. Freitas, M. Stuefer, and J. Fast (2010), Inclusion of biomass burning in WRF-Chem: Impact of wildfires on weather forecasts, *Atmos. Chem. Phys. Discuss.*, *10*, 30,613–30,650, doi:10.5194/acpd-10-30613-2010.

Gustafson, W. I., Jr., E. G. Chapman, S. J. Ghan, R. C. Easter, and J. D. Fast (2007), Impact on modeled cloud characteristics due to simplified treatment of uniform cloud condensation nuclei during NEAQS 2004, *Geophys. Res. Lett.*, *34*, L19809, doi:10.1029/2007GL030021.

Hong, S.-Y., and J.-O. J. Lim (2006), The WRF single-moment 6-class microphysics scheme (WSM6), *J. Korean Meteorol. Soc.*, *42*, 129–151.

Horowitz, L. W., et al. (2003), A global simulation of tropospheric ozone and related tracers: Description and evaluation of MOZART, version 2, *J. Geophys. Res.*, *108*(D24), 4784, doi:10.1029/2002JD002853.

Huang, Y., W. L. Chameides, and R. E. Dickinson (2007), Direct and indirect effects of anthropogenic aerosols on regional precipitation over East Asia, *J. Geophys. Res.*, *112*, D03212, doi:10.1029/2006JD007114.

Janjic, Z. I. (1996), The surface layer in the NCEP Eta Model, paper presented at 11th Conference on Numerical Weather Prediction, Am. Meteor. Soc., Norfolk, Va.

Jensen, E. J., and O. B. Toon (1992), The potential effects of volcanic aerosols on cirrus cloud microphysics, *Geophys. Res. Lett.*, *19*(17), 1759–1762, doi:10.1029/92GL01936.

Khain, A., N. Cohen, B. Lynn, and A. Pokrovsky (2008a), Possible aerosol effects on lightning activity and structure of hurricanes, *J. Atmos. Sci.*, *65*, 3652–3677, doi:10.1175/2008JAS2678.1.

Khain, A. P., N. BenMoshe, and A. Pokrovsky (2008b), Factors determining the impact of aerosols on surface precipitation from clouds: An attempt at classification, *J. Atmos. Sci.*, *65*, 1721–1748, doi:10.1175/2007JAS2515.1.

Lamb, H. H. (1970), Volcanic dust in the atmosphere, with a chronology and assessment of its meteorological significance, *Philos. Trans. R. Soc. London, Ser. A*, *266*, 425–533, doi:10.1098/rsta.1970.0010.

Leroy, D., W. Wobrock, and A. I. Flossmann (2009), The role of boundary layer aerosol particles for the development of deep convective clouds: A high-resolution 3D model with detailed (bin) microphysics applied to CRYSTAL-FACE, *Atmos. Res.*, *91*, 62–78, doi:10.1016/j.atmosres.2008.06.001.

Leung, F.-Y. T., J. A. Logan, R. Park, E. Hyer, E. Kasischke, D. Streets, and L. Yurganov (2007), Impacts of enhanced biomass burning in the boreal forests in 1998 on tropospheric chemistry and the sensitivity of model results to the injection height of emissions, *J. Geophys. Res.*, *112*, D10313, doi:10.1029/2006JD008132.

Lim, K.-S. S., S.-Y. Hong, S. S. Yum, J. Dudhia, and J. B. Klemp (2011), Aerosol effects on the development of a supercell storm in a double-moment bulk-cloud microphysics scheme, *J. Geophys. Res.*, *116*, D02204, doi:10.1029/2010JD014128.

Lin, Y., and K. E. Mitchell (2005), The NCEP stage II/IV hourly precipitation analyses: Development and applications, paper presented at 19th Conference on Hydrology, Am. Meteor. Soc., San Diego, Calif.

Lin, Y.-L., R. D. Farley, and H. D. Orville (1983), Bulk parameterization of the snow field in a cloud model, *J. Clim. Appl. Meteorol.*, *22*, 1065–1092, doi:10.1175/1520-0450(1983)022<1065:BPOTSF>2.0.CO;2.

Liu, S. C., et al. (1996), Model study of tropospheric trace species distributions during PEM-West A, *J. Geophys. Res.*, *101*, 2073–2086, doi:10.1029/95JD02277.

Liu, Y., P. H. Daum, and R. L. McGraw (2005), Size truncation effect, threshold behavior, and a new type of autoconversion parameterization, *Geophys. Res. Lett.*, *32*, L11811, doi:10.1029/2005GL022636.

Lu, R., and R. P. Turco (1994), Air pollutant transport in a coastal environment. Part I: Two-dimensional simulations of sea-breeze and mountain effects, *J. Atmos. Sci.*, *51*, 2285–2308, doi:10.1175/1520-0469(1994)051<2285:APTIAC>2.0.CO;2.

Mlawer, E. J., S. J. Taubman, P. D. Brown, M. J. Iacono, and S. A. Clough (1997), Radiative transfer for inhomogeneous atmosphere: RRTM, a validated correlated-k model for the long- wave, *J. Geophys. Res.*, *102*(D14), 16,663–16,682, doi:10.1029/97JD00237.

Molinié, J., and C. A. Pontikis (1995), A climatological study of tropical thunderstorm clouds and lightning frequencies on the French Guyana Coast, *Geophys. Res. Lett.*, *22*(9), 1085–1088, doi:10.1029/95GL01036.

Ntelekos, A. A., J. A. Smith, L. J. Donner, J. D. Fast, W. I. Gustafson Jr., E. G. Chapman, and W. F. Krajewski (2009), The effects of aerosols on intense convective precipitation in the northeastern US, *Q. J. R. Meteorol. Soc.*, *135*, 1367–1391, doi:10.1002/qj.476.

Pfister, G. G., et al. (2011), Characterizing summertime chemical boundary conditions for airmasses entering the US West Coast, *Atmos. Chem. Phys.*, *11*, 1769–1790, doi:10.5194/acp-11-1769-2011.

Radke, L. F., J. A. Coakley Jr., and M. D. King (1989), Direct and remote sensing observations of the effects of ships on clouds, *Science*, *246*, 1146–1149, doi:10.1126/science.246.4934.1146.

Ramanathan, V., P. J. Crutzen, J. T. Kiehl, and D. Rosenfeld (2001), Aerosols, climate and the hydrological cycle, *Science*, *294*, 2119–2124, doi:10.1126/science.1064034.

Robock, A. (2000), Volcanic eruptions and climate, *Rev. Geophys.*, *38*, 191–219, doi:10.1029/1998RG000054.

Rosenfeld, D. (2000), Suppression of rain and snow by urban air pollution, *Science*, *287*, 1793–1796, doi:10.1126/science.287.5459.1793.

Rosenfeld, D., U. Lohmann, G. B. Raga, C. D. O'Dowd, M. Kulmala, S. Fuzzi, A. Reissell, and M. O. Andreae (2008), Flood or drought: How do aerosols affect precipitation?, *Science*, *321*, 1309–1313, doi:10.1126/science.1160606.

Sassen, K., et al. (1995), The 5–6 December 1991 FIRE IFO II Jet Stream Cirrus Case Study: Possible influences of volcanic aerosols., *J. Atmos. Sci.*, *52*, 97–123.

Schell, B., I. J. Ackermann, H. Hass, F. S. Binkowski, and A. Ebel (2001), Modeling the formation of secondary organic aerosol within a comprehensive air quality model system, *J. Geophys. Res.*, *106*, 28,275–28,293, doi:10.1029/2001JD000384.

Sessions, W. R., H. E. Fuelberg, R. A. Kahn, and D. M. Winker (2010), An investigation of methods for injecting emissions from boreal wildfires using WRF-Chem during ARCTAS, *Atmos. Chem. Phys. Discuss.*, *10*, 26,551–26,606, doi:10.5194/acpd-10-26551-2010.

Skamarock, W. C., J. B. Klemp, J. Dudhia, D. O. Gill, D. M. Barker, W. Wang, and J. G. Powers (2008), A description of the advanced research WRF version 3, *NCAR Tech. Note, NCAR/TN-475+STR*, 125 pp., Natl. Cent. for Atmos. Res, Boulder, Colo. [Available at http://www.mmm.ucar.edu/wrf/users/docs/arw_v3.pdf.]

Stocks, B. J., et al. (2003), Large forest fires in Canada, 1959–1997, *J. Geophys. Res.*, *108*(D1), 8149, doi:10.1029/2001JD000484.

Stockwell, W. R., P. Middleton, J. S. Chang, and X. Tang (1990), The second-generation regional acid deposition model chemical mechanism for regional air quality modeling, *J. Geophys. Res.*, *95*, 16,343–16,367, doi:10.1029/JD095iD10p16343.

Stohl, A., et al. (2006), Pan-Arctic enhancements of light absorbing aerosol concentrations due to North American boreal forest fires during summer 2004, *J. Geophys. Res.*, *111*, D22214, doi:10.1029/2006JD007216.

Tao, W.-K., X. Li, A. Khain, T. Matsui, S. Lang, and J. Simpson (2007), Role of atmospheric aerosol concentration on deep convective precipitation: Cloud-resolving model simulations, *J. Geophys. Res.*, *112*, D24S18, doi:10.1029/2007JD008728.

van den Heever, S. C., G. Carrio, W. Cotton, P. DeMott, and A. Prenni (2006), Impacts of nucleating aerosol on Florida storms. Part I: Mesoscale simulations, *J. Atmos. Sci.*, *63*, 1752–1775, doi:10.1175/JAS3713.1.

Wang, C. (2005), A modelling study of the response of tropical deep convection to the increase of cloud condensational nuclei concentration: 1. Dynamics and microphysics, *J. Geophys. Res.*, *110*, D21211, doi:10.1029/2004JD005720.

Warneke, C., et al. (2006), Biomass burning and anthropogenic sources of CO over New England in the summer 2004, *J. Geophys. Res.*, *111*, D23S15, doi:10.1029/2005JD006878.

Williams, E., et al. (2002), Contrasting convective regimes over the Amazon: Implications for cloud electrification, *J. Geophys. Res.*, *107*(D20), 8082, doi:10.1029/2001JD000380.

Winner, D. A., G. R. Cass, and R. A. Harley (1995), Effect of alternative boundary conditions on predicted ozone control strategy: A case study in Los Angeles area, *Atmos. Environ.*, *29*(33), 3451–3464, doi:10.1016/1352-2310(95)00222-K.

Wotawa, G., and M. Trainer (2000), The influence of Canadian forest fires on pollutant concentrations in the United States, *Science*, *288*, 324–328, doi:10.1126/science.288.5464.324.

Zhang, H., G. M. McFarquhar, S. M. Saleeby, and W. R. Cotton (2007), Impacts of Saharan dust as CCN on the evolution of an idealized tropical cyclone, *Geophys. Res. Lett.*, *34*, L14812, doi:10.1029/2007GL029876.

M. S. Pritchard, L. M. Russell, and Z. Zhao, Scripps Institution of Oceanography, University of California, San Diego, 9500 Gilman Dr., La Jolla, CA 92093-0532, USA. (lmrussell@ucsd.edu)